

# Long-term spatio-temporal evolution of the dust distribution in **dusty** argon rf plasmas

Carsten Killer,<sup>1, a)</sup> Franko Greiner,<sup>2</sup> Sebastian Groth,<sup>2</sup> Benjamin Tadsen,<sup>2</sup> and André Melzer<sup>1</sup>

<sup>1)</sup>*Institut für Physik, Ernst-Moritz-Arndt-Universität, 17489 Greifswald, Germany*

<sup>2)</sup>*IEAP, Christian-Albrechts-Universität, 24098 Kiel, Germany*

The 3D dust distribution in dense dust clouds confined in argon rf plasmas is measured by a computed tomography (CT) technique based on the extinction of visible light. On the one hand, clouds of micron-sized particles were created by injecting standardized plastic particles into the plasma. On the other hand, **sub-micron sized** dust with well-defined properties is grown *in situ* in an argon acetylene mixture. Once created, both kinds of dust clouds decay in the course of minutes to hours. This decay is monitored by CT measurements. It is revealed that micro-dust clouds feature a drastic change of the dust distribution due to a size reduction of the dust. **Dust clouds of sub-micron particles**, in contrast, show a strong variation of the overall dust density while the relative dust distribution remains nearly unchanged. The evolution of the overall dust density is subject to two effects: the loss of particles due to an imperfect confinement and the reduction of the dust size via etching.

## I. INTRODUCTION

With an appropriate confinement, large amounts of dust particles can be trapped in low temperature rf plasmas where they form dense clouds. The dust can either be specifically injected into the plasma or grow *in situ* when the plasma contains a chemically reactive species. In the plasma, the dust particles attain negative electric charges and can therefore be confined in the presence of electric fields.

In experiments on micron-sized dust, usually standardized monodisperse plastic particles are employed, which acquire high negative electric charges of the order of  $10^3$  to  $10^4$  elementary charges. Ensembles of such particles can form different manifestations of strongly coupled Coulomb systems stretching from 2D layers<sup>1,2</sup> via finite 3D clusters<sup>3</sup> to large clouds that fill almost the entire plasma volume<sup>4–8</sup>. Due to the dominant influence of gravity on micron-sized particles, creating such a cloud requires either weightlessness conditions<sup>4,6,7</sup> or the compensation of gravity, e.g. by thermophoretic levitation<sup>5,8</sup>.

While experiments on micron-sized dust often focus on fundamental research since phenomena related to non-linear dynamics and strong coupling can be studied on the level of individual particles<sup>9,10</sup>, nano-dusty plasmas are of high relevance for technological plasmas<sup>11</sup>. On the one hand, the unwanted growth of nanoparticles in such plasmas can be harmful to the plasma process since the dust growth affects the plasma parameters<sup>12–18</sup> and, in addition, dust particles may damage the object that is being processed (e.g. delicate silicon structures for the semi-conductor industry). On the other hand, the controlled growth of nano-dust can in some situations improve the efficiency of the plasma processing, e.g. in the production of polymorphous solar cells<sup>19</sup>. Hence, the formation of nanoparticles in low temperature rf plasmas

has been widely studied<sup>20–23</sup>. Lately, the structure and evolution of dense nano-dust clouds attracted growing interest<sup>24–27</sup>. While most works focus on the growth dynamics, the behaviour of (supposedly) static nano-dust clouds whose growth was stopped by turning off the reactive gas feed remains largely unstudied. Recently, evidence of a dust size reduction via an etching-like process was observed in argon rf plasmas containing carbonaceous nano-dust which had been grown by admixing acetylene for a certain time span<sup>28</sup>. In addition, the dust density was found to diminish on the time scale of some minutes due to a loss of dust particles<sup>28,29</sup>.

The phenomenon of dust size and/or mass reduction has also been observed for micron-sized plastic particles: In oxygen plasmas, melamine formaldehyde (mf) particles were subject to etching by reactive oxygen radicals<sup>30,31</sup>. Even in (chemically inert) argon plasmas, mf particle properties are affected by exposure to the plasma: Carstensen et al. observed a mass loss of mf particles in the plasma which was attributed to outgassing effects<sup>32</sup>. In large clouds of mf particles confined in argon plasmas, Killer et al. found both a decrease of the dust size and mass density<sup>33</sup>. Since the confinement of these clouds is created by a superposition of forces that depend on the dust size, charge, and mass; changes in one or more of these fundamental dust properties also affect the dust density distribution in the cloud.

In this paper, a tomographic method based on light extinction is used to determine and compare the 3D dust distribution in **dust clouds of both micron- and sub-micron-sized particles**. The time evolution of the dust distribution gives insight into the physical mechanisms which determine the dust confinement and govern the decay of the clouds. **For readability, we will refer to the sub-micron particles as nano-particles in this paper even if their radius is as large as 200 nm.**

---

<sup>a)</sup>present address: Max-Planck-Institut für Plasmaphysik, 17491 Greifswald, Germany; Electronic mail: carsten.killer@ipp.mpg.de

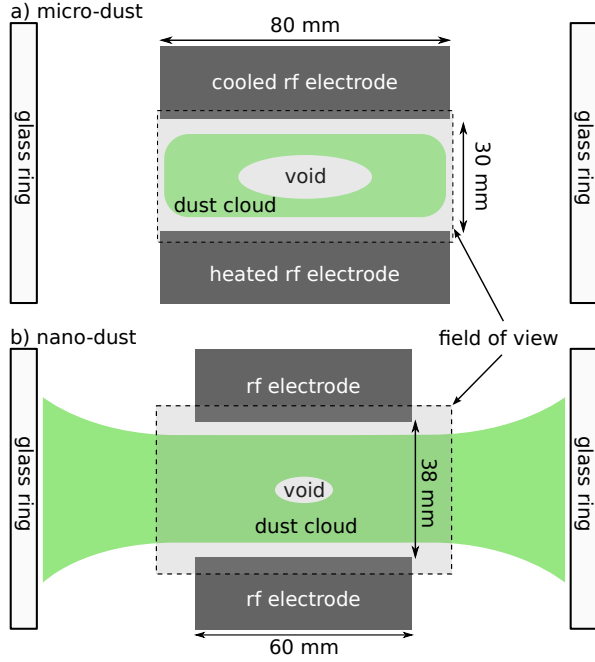


FIG. 1. Front view sketch of the basic discharge geometries. The area occupied by the dust cloud is colored green.

## II. EXPERIMENTAL SETUP AND DIAGNOSTICS

The presented experiments were performed in capacitively coupled radio frequency discharges (13.56 MHz) in a symmetric parallel plate configuration. A glass ring (outer diameter 170 mm) is utilized as the side wall of the plasma chamber in order to provide 360° optical access to the dust clouds in the horizontal plane which is required for the tomographic experiments. The details of the specific discharge geometry are different for the micro- and nano-dust experiments as sketched in Fig. 1. In this section, the respective experimental setups and the diagnostics will be briefly presented.

### A. Micro-dust experiments

Clouds of micron-sized particles have been confined in a plasma chamber similar to the one described in Ref.<sup>34</sup> which features a pair of circular electrodes with a diameter of 80 mm and a discharge gap of 30 mm. The discharge is ignited in argon at a pressure of about 20 Pa at low discharge powers of the order of 1 W. The dust particles are made of melamine formaldehyde (mf) and have a radius of  $a_d = 1.78 \mu\text{m}$ . Using electromagnetic shakers, large amounts of dust particles can be introduced into the plasma. To create a vertically extended dust cloud, gravity is compensated by the thermophoretic force which arises due to a temperature gradient in the neutral gas. This gradient is created by setting the temperature of the electrodes to 5°C (upper electrode) and 36°C (lower electrode) in order to provide an optimal levitation for

the particles used here<sup>5</sup>.

From experiments in the same plasma chamber under similar conditions it is known that the dust size constantly diminishes when the dust is confined in the plasma<sup>33</sup>. This process is attributed to a combined action of outgassing of volatile components from the dust and etching via reactive impurities (e.g. oxygen radicals). The dust size evolution was studied in Ref.<sup>33</sup> by measuring the angle-resolved Mie scattering intensities from which the dust size can be directly inferred. These experiments are comparable to the ones presented in this article since they were performed using the same kind of dust particles in the same plasma chamber under similar plasma conditions. We therefore assume that the mean size loss rate of 0.04 nm/s which was found in Ref.<sup>33</sup> also applies to the experiments presented here.

### B. Nano-dust experiments

Nanometer-sized particles were grown and studied in a plasma chamber similar to the one described in Ref.<sup>29</sup>. The circular electrodes have a diameter of 60 mm and are separated by a discharge gap of 38 mm. The discharge is ignited in argon at a pressure of 24 Pa with a plasma power of 8 W. The dust growth starts at  $t = 0$  when acetylene ( $\text{C}_2\text{H}_2$ ) is admixed to the argon gas at a ratio of 20 % while the total flow rate is kept constant at 8 sccm. When the acetylene flow is switched off the dust growth stops, resulting in a nano-dust cloud with a homogeneous size distribution<sup>24</sup>.

The dust size is monitored by a combination of Mie ellipsometry and an imaging Mie (I-Mie) technique. The Mie ellipsometry provides the dust size and the refractive index at one spatial position within the cloud using the CRAS-Mie method introduced in Ref.<sup>28</sup>. The I-Mie measurements provide the spatial dust size distribution on a

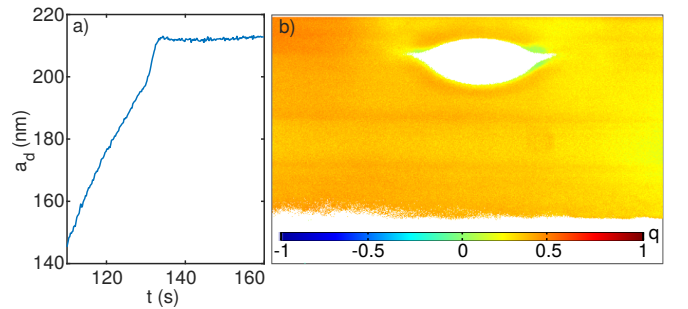


FIG. 2. a) Dust growth measured by Mie ellipsometry<sup>28</sup> at one position in the dust cloud. The acetylene supply is switched off at  $t = 129$  s. b) The size distribution measured by I-Mie<sup>24</sup> confirms that the cloud is approximately monodisperse (image taken at  $t = 140$  s). Here,  $q$  is the second Stokes parameter  $Q = I_{\parallel} - I_{\perp}$  normalized by total polarized intensity  $I_p$  which is a suitable quantity to determine the relative dust size distribution in a wide size range. The dust size variation in this image is smaller than 10 nm.

qualitative level in a wide size range<sup>24</sup>. Using different laser colors for technical reasons (665 nm for Mie ellipsometry and 532 nm for I-Mie) is unproblematic since the spectral dependence of the dust refractive index is rather weak<sup>35</sup>.

A typical growth curve determined by CRAS-Mie ellipsometry is shown in Fig. 2 a). The acetylene flow was switched on at  $t = 0$ , initiating the growth process. Shortly after the acetylene supply is switched off at  $t = 129$  s the growth stops, resulting in a constant dust radius of about 210 nm. The relative size distribution measured by I-Mie in Fig. 2 b) confirms that the nano-dust is approximately monodisperse.

Due to the spatial requirements of the different diagnostics, it was not possible to perform the dust size measurements simultaneously with the tomographic experiments. Hence, the experiments were repeated under identical conditions. The rf voltage and the total gas pressure were found to be suitable characteristics which can be used as a reference for a common time axis in order to combine the dust size and dust density measurements.

### C. Tomography

The tomographic measurements for the dust density determination are based on the experimental setup presented in Ref.<sup>36</sup>. The dust cloud is trans-illuminated by an extended LED panel emitting white light. A CCD camera equipped with a bi-telecentric lens is located opposite to the LED panel, recording the transmitted light. From the light extinction due to scattering and absorption by the dust the line-integrated dust density can be determined. This process can adequately be described by the simple Beer-Lambert law under the assumption that multiple scattering can be neglected, which is justified in the optically very thin micro-dust clouds and also applies in most nano-dusty situations where the optical depth is of the order of 0.3. When the transmitted light intensity  $I$  and the incident intensity  $I_0$  have been measured, the dust density  $n_d$  can then be extracted from the Beer-Lambert law  $I = I_0 \exp(-n_d \sigma l)$  where  $l$  is the optical path length and  $\sigma$  is the extinction cross section of a single dust particle. This property is calculated from standard Mie scattering theory and depends on the dust size as well as the refractive index.

To determine the local dust density in a cloud with an arbitrary density distribution, the line integrated measurements are performed from many different angles in analogy to a CT known from medical imaging. The local dust density distribution is then reconstructed using the inverse Radon transform<sup>37</sup> (here, the implementation of MATLAB's Image Processing Toolbox has been used).

The temporal resolution of the CT technique is limited by the necessity to move the camera and LED panel on a rotating stage. Since a full rotation takes about 10 s, only static properties of the dust clouds are studied here. The spatial resolution is defined by the camera

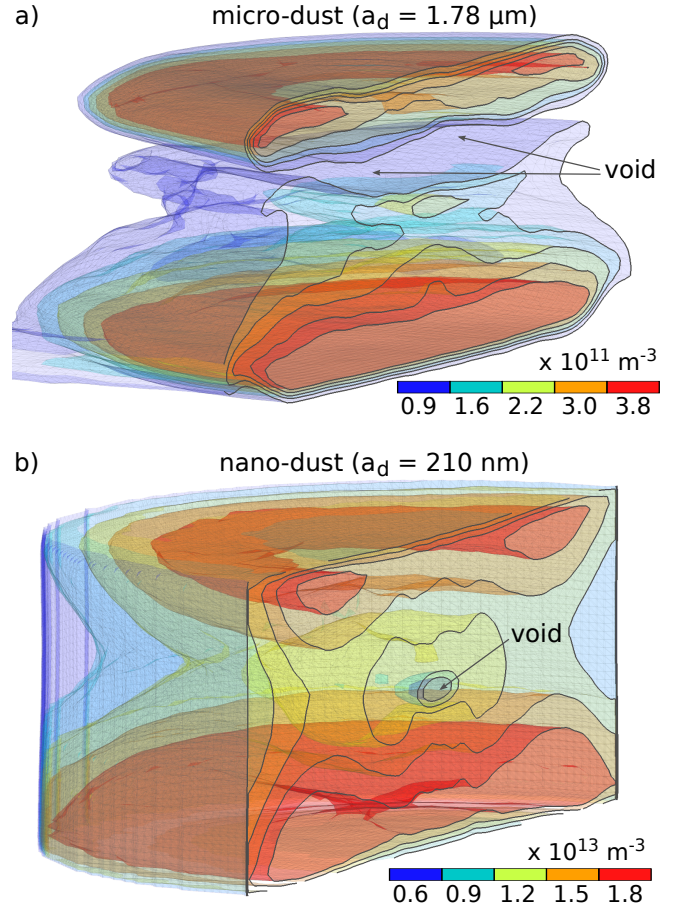


FIG. 3. The 3D dust density distribution in a) a micro-dust cloud and b) a nano-dust cloud directly after a) injection of the dust and b) after the growth is stopped. The colored iso-surfaces connect points of equal dust density. For clarity, only one half of the cloud is shown, emphasizing the structure in the central cutting edge. The cloud dimensions are (diameter  $\times$  height): 77 mm  $\times$  23 mm for the micro-dust cloud and 82 mm  $\times$  30 mm for the nano-dust cloud. The color scaling is different for both clouds since the dust density differs by two orders of magnitude.

properties (640  $\times$  480 px with a conversion ratio of about 7.8 px/mm) and the angular step width, which should be smaller than  $2^\circ$ . The effective resolution is of the order of 0.5 mm due to the intrinsic filtering provided by sophisticated implementations of the inverse Radon transform<sup>37</sup>.

### III. DUST CLOUD STRUCTURE

The initial 3D dust density distribution directly after the clouds have been created is presented in Fig. 3 a) for a micro-dust clouds (directly after dust injection) and b) for a nano-dust cloud (after the nanoparticle growth was stopped). At a first glance, both systems share similar features: The dust density is highest in the upper and lower edge region of the cloud and a dust-free void is

found in the center. In both cases, the areas of highest dust densities form a toroidal shape in the upper part of the cloud while it resembles a rather homogeneous, pancake-like structure in the bottom region.

While the basic structure of both systems is comparable, a closer inspection of the cloud symmetry reveals significant differences. In general, a dust cloud that is purely confined by plasma related forces is expected to be cylindrically and vertically symmetric due to the symmetric nature of the plasma geometry (see e.g. micro-dust clouds under microgravity conditions<sup>6</sup>). The micro-dust cloud in Fig. 3 a) features a significant vertical asymmetry as well as smaller deviations from cylindrical symmetry. The up-down asymmetry can be attributed to the delicate balance of gravitational and thermophoretic force which dominates the vertical confinement since these forces are much larger than the electric field force and ion drag force. Already a small disparity between these force can lead to a sedimentation [in Fig. 3 a), the gravitational force seems to be not fully compensated by the upwards directed thermophoresis]. The deviations from cylindrical symmetry can probably be attributed to unwanted horizontal components of the thermophoretic force field. This side effect might arise from temperature gradients on the electrode surfaces and between electrodes and walls which cannot be completely suppressed due to inherent technical limitations of the water circulation system that controls the electrode temperatures.

The nano-dust cloud in Fig. 3 b) reveals a much higher degree of both vertical and cylindrical symmetry. The cylindrical dust density distribution entirely reflects the confinement by the symmetric geometry of the plasma-related forces (electric field force, ion drag force). Although gravity is not a dominant force for the nanometer-sized particles, the vertical dust distribution is slightly shifted towards the lower half of the cloud, revealing a weak gravity-induced sedimentation. The central dust-free void is quite small and is surrounded by a larger region of a relatively low dust density. The sharp outer edge of the dust cloud stems from the fact that the dust cloud extends beyond the field of view, see Fig. 1 b).

#### IV. DUST CLOUD EVOLUTION

To study the evolution of the dust distribution in micro- and nano-dust clouds, series of CT measurements have been performed over the course of 30 - 100 min. First, the respective dust cloud was created by injecting or growing the dust. Then, CT measurements were repeatedly taken while all experimental parameters were kept constant. Some representative stages of the dust cloud evolution are presented in Fig. 4.

The evolution of a micro-dust cloud is shown in the upper row of Fig. 4 where the first panel is identical to the image in Fig. 3 a). In the course of almost two hours a drastic change of the dust distribution can

be observed. The vertical density distribution clearly shifts towards the upper part of the cloud. In the last panel, almost no dust is left below the (now very large) void. This behaviour can be attributed to the significant reduction of the dust size and mass density which was observed in the same plasma chamber under similar conditions<sup>33</sup>. With a decreasing dust mass the balance between thermophoretic force (scaling with  $d^2$ ) and gravitational force (scaling with  $d^3$ ) is shifted in favor of the (upwards directed) thermophoretic force. In the further evolution the dust gets compressed into a flat pancake-like structure in the upper sheath. The deviations from cylindrical symmetry appear to become smaller during time evolution. It is reasonable to assume that the much more stressed confinement situation in the later evolution stages conceals the finer inhomogeneities of the thermophoretic force field.

The evolution of the nano-dust cloud in the middle row of Fig. 4 reveals a different behaviour. The overall dust density decreases drastically in the course of time while the relative dust distribution remains nearly unchanged. The latter observation is confirmed by the bottom row of Fig. 4, where the same data are shown with a normalized color scaling. While the cylindrical dust distribution does not change over time, a small shift of the dust density along the vertical direction towards the upper part of the cloud is observed. In analogy to the micro-dust clouds, this might be attributed to a size and/or mass reduction of the nanoparticles in the plasma which weakens the gravity-induced sedimentation.

Besides the changes of the relative dust distribution, both systems feature a reduction of the overall dust number. To approach this phenomenon, the total number of particles in a dust cloud  $N_d$  is calculated by simply integrating the dust density over the entire cloud volume. The time evolution of the total particle number is presented in Fig. 5 a) for micro-dust and b) for nano-dust clouds. As expected from the density illustrations in Figs. 3 and 4, the total number of dust particles is much larger in the nano-dust cloud, resulting in a different scaling of the vertical axis.

The micro-dust cloud in Fig. 5 a) features a steady decrease of  $N_d$  by a factor of 2 over almost two hours. While the open symbols represent the dust density under the assumption of a constant dust size, the square symbols account for a decreasing dust size using the etch rate of 0.04 nm/s which was found under similar conditions in Ref.<sup>33</sup>. This size reduction affects the extinction cross section  $\sigma$  and therefore the reconstructed dust density. Comparing both datasets clearly illustrates that the dust etching is significant for the density analysis. At the end of the measurement series, almost two hours after dust injection, accounting for the dust etching already results in a 30 % larger dust density. Furthermore, the segmentation of the dust cloud into regions of slightly different dust sizes (which was also found in Ref.<sup>33</sup>) will in principle also affect the relative dust density distribution in micro-dust clouds since the dust size is not homoge-



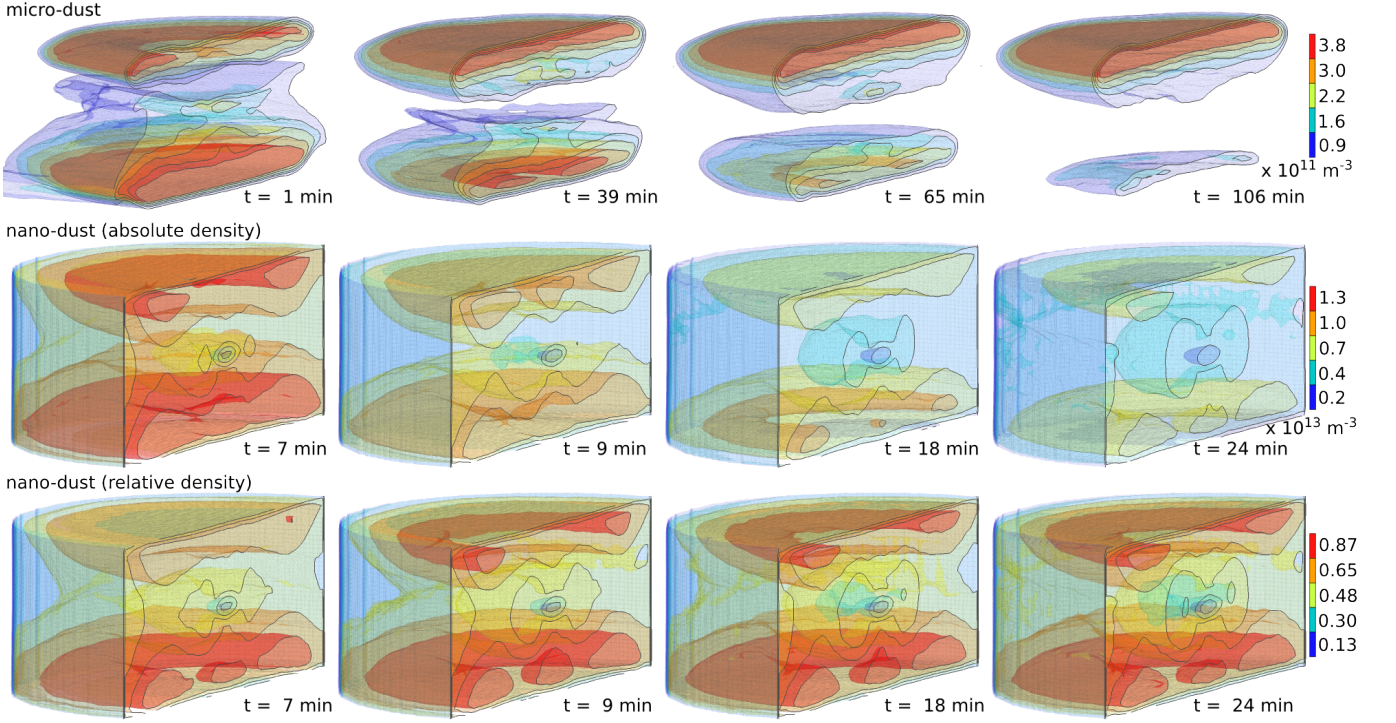


FIG. 4. Time evolution of the 3D dust density distribution in micro-dust (upper row) and nano-dust clouds (middle and bottom row) assuming a constant dust size throughout the measurement series. The color scaling is kept constant in the upper and middle row. In the bottom row, the color scaling is normalized to the maximal dust density in each panel, revealing the evolution of the relative dust distribution. (see supplementary online material for the animated evolution of the full measurement series)

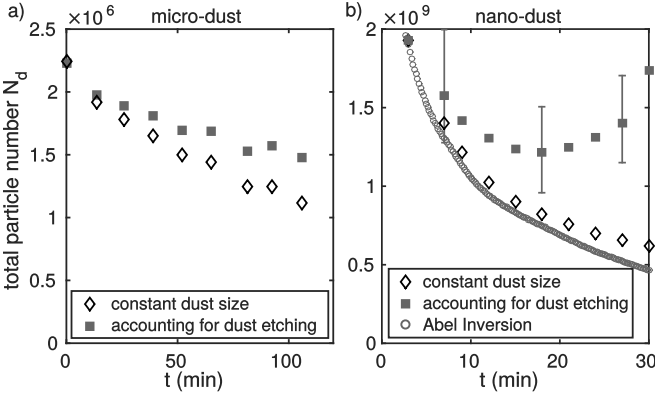


FIG. 5. Time evolution of the total particle number in a) a micro-dust cloud and b) in the observation volume of a nano-dust cloud. The grey squares have been obtained in a) by assuming an etching rate of  $0.04 \text{ nm/s}$ <sup>33</sup> and in b) based on the Mie ellipsometry results shown in Fig. 6. The open circles are derived from Abel inversion of single extinction images which were acquired with a higher temporal resolution (for clarity, only the dataset based on a constant dust size is shown here).

neously distributed. This effect is, however, quite small and will not be addressed here since it requires to perform CT and Mie scattering measurements in 3D simultaneously, which is experimentally challenging.

The nano-dust cloud in Fig. 5 b) features, in com-

parison, a much stronger decrease of the total particle number when a constant dust size is assumed. In just 30 minutes,  $N_d$  drops to about one third of the initial dust density. Such a drastic decay was already observed in previous investigations under similar experimental conditions<sup>29</sup>. An attempt to explain this behaviour involves the growth dynamics: When the accretion phase in the growth process begins, the number of dust particles does not change anymore<sup>29,38</sup>. While this fixed quantity of dust particles grows by accretion of molecules, the negative charge on the dust particles becomes larger, resulting in a stronger repelling interaction of the dust particles and consequently a larger inter-particle spacing. It could therefore be conjectured that too many dust particles grow which the plasma cannot confine in the long term. Hence, the excess of dust particles is lost from the confinement. Such a process was visible to the bare eye during the measurements in the area close to the outer glass ring, well outside the camera's field of view.

This mechanism is, however, not the full story. The accompanying Mie ellipsometry measurements indicate a substantial etching of the nano-dust which was also observed in previous experiments under similar conditions<sup>28</sup>. The time evolution of the dust size measured in our experiments is presented in Fig. 6 and was calculated under the assumption that the refractive index of the dust does not change upon etching. Incorporating

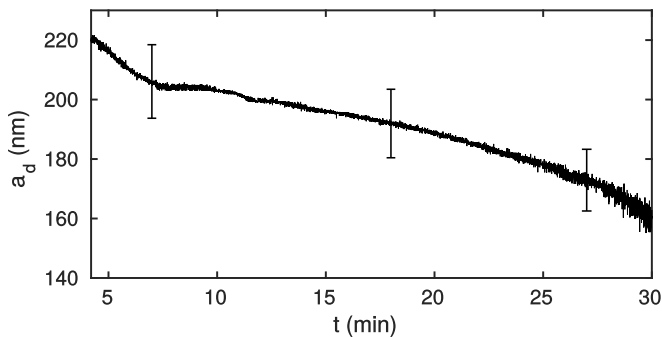


FIG. 6. Time evolution of the nano-dust particle size obtained by Mie ellipsometry assuming a constant dust refractive index.

the dynamic dust size of Fig. 6 into the dust density reconstruction, we obtain the dataset represented by the square symbols in Fig. 5 b). Surprisingly, after an initial decrease, the total number of dust particles starts to increase after 15 minutes and has almost reached the initial value after 30 minutes. This behaviour follows from the fact that the extinction cross section  $\sigma$  (which is a function of the dust size) drops faster than the optical depth, resulting in an apparent increase of the dust density.

To study the influence of uncertainties in the dust size determination on the reconstructed dust density, three representative error bars are shown in Fig. 6 which illustrate the typical maximum uncertainty of 6 % attributed to our CRAS-Mie method<sup>28</sup>. This error follows from uncertainties of the refractive index and can therefore be regarded as a systematic error since the refractive index is assumed to be constant over time. The effect of this uncertainty on the dust density is consequently represented by corresponding error bars in Fig. 5 b). The fact that the error bars in Fig. 5 b) are much larger (on a relative scale) compared to the ones in Fig. 6 illustrates that a small variation of the dust size can strongly affect the extinction cross section and therefore the resulting dust density. However, our observation of an increasing particle number after 15 minutes is unaffected for all values of the refractive index in the considered error range.

As an attempt to explain the unexpected behavior of the  $N_d(t)$  curve in Fig. 5b), it could be conjectured that the etching-induced size reduction results in smaller dust charges per particle and hence a weaker dust-dust interaction. This way, the electrostatic pressure<sup>39</sup> in the cloud decreases and dust from the area outside the field of view [see Fig. 1 b)] can enter into the central plasma volume between the electrodes due to the inwards directed confining force balance. This proposition conforms with the observation of a small shift in the radial dust density distribution towards the radially outer parts of the nano-dust cloud in the course of time. For a thorough understanding of such a mechanism, however, further complications have to be considered: As an example, a variation of the dust density will also affect the Havnes

parameter<sup>40,41</sup> in our highly electron-depleted plasma<sup>42</sup>. As a consequence, the effective dust charge and therefore the electrostatic dust pressure change, resulting in a complex feedback loop. **A direct influence of plasma forces such as the electric field force or ion drag force on the particle transport is probably less relevant since the overall structure of the dust cloud remains nearly unchanged during this process.**

This open question might be resolved by improving the experimental setup in a way that the dust cloud is confined entirely in the field of view, which will provide definite information about the total dust distribution and dust transport. One way to achieve this is to perform the experiments in the presence of a strong magnetic field<sup>29</sup>, which, however, alters the plasma properties and therefore the confinement.

Finally, the high cylindrical symmetry of the nano-dust clouds is also demonstrated by the circles in Fig. 5 b). There, the total particle number has been calculated from a measurement series under identical experimental conditions where instead of a tomography just extinction images from a single angular position were taken. Assuming cylindrical symmetry of the dust cloud, the dust density distribution is obtained using the inverse Abel transform<sup>43,44</sup>. Analogous to the CT measurements, the total number of dust particles in the cloud  $N_d$  is determined by integrating the dust density distribution over the entire cloud volume. The resulting dataset represented by the circles in Fig. 5 b) shows a good agreement with the data points from the tomography, and, with a much higher temporal resolution, further indicating that the cloud is very symmetric (for clarity, only the curve assuming a constant dust size is shown, corresponding to the open diamonds). For very symmetric dust clouds, the Abel inversion approach therefore offers a much faster temporal resolution (compared to CT) which might be used to study dynamic phenomena such as the spatial dynamics of particle growth in reactive plasmas or self-excited dust density waves<sup>42</sup>.

## V. SUMMARY

We have presented tomographic measurements of the 3D dust density distribution in micro- and nano-dust clouds confined in argon rf plasmas. The long term evolution of the dust distribution in static dust clouds was studied by repeated CT measurements. While both nano- and micro-dust clouds share a similar basic structure, the nano-dust clouds have a much higher degree of both vertical and cylindrical symmetry. The micro-dust clouds are dominated by the delicate balance of gravity and thermophoresis which mainly forms the vertical dust confinement and therefore affects the vertical symmetry. The small but steady size reduction of the micro-particles in the plasma results in a strong vertical shift of the dust density. The relative dust distribution in the nano-dust clouds, in contrast, remains almost unchanged

in the course of time while the absolute density changes drastically. It has been shown that the size reduction of micro- and nano-particles in the plasma (e.g. via etching) has a considerable effect on the reconstructed dust density. Incorporating the etching process into the dust density analysis of the nano-dust clouds suggests that after an initial decrease the total dust density starts to increase again. This observation might be explained by the balance between the confining forces and the electrostatic dust pressure and the fact that there is a reservoir of nanoparticles outside the field of view. Finally, the very symmetric nature of the nano-dust clouds allows to reduce the measurement effort to just one projection from which the local dust density is derived via the inverse Abel transform, which offers a faster time resolution.

## ACKNOWLEDGMENTS

Financial support from the Deutsche Forschungsgemeinschaft via SFB-TR24 (projects A2 and A3) and from the German Aerospace Center DLR, contract No. 50WM1538 is gratefully acknowledged. We thank Volker Rohwer for technical assistance during the CT campaign of CK in Kiel.

- <sup>1</sup>J. H. Chu and L. I. Phys. Rev. Lett. **72**, 4009 (1994).
- <sup>2</sup>H. Thomas, G. E. Morfill, V. Demmel, J. Goree, B. Feuerbacher, and D. Möhlmann, Phys. Rev. Lett. **73**, 652 (1994).
- <sup>3</sup>O. Arp, D. Block, A. Piel, and A. Melzer, Phys. Rev. Lett. **93**, 165004 (2004).
- <sup>4</sup>G. E. Morfill, H. Thomas, U. Konopka, H. Rothermel, M. Zuzic, A. Ivlev, and J. Goree, Phys. Rev. Lett. **83**, 1598 (1999).
- <sup>5</sup>H. Rothermel, T. Hagl, G. Morfill, M. Thoma, and H. M. Thomas, Phys. Rev. Lett. **89**, 175001 (2002).
- <sup>6</sup>A. P. Nefedov, G. E. Morfill, V. E. Fortov, H. M. Thomas, H. Rothermel, T. Hagl, A. V. Ivlev, M. Zuzic, B. A. Klumov, A. M. Lipaev, V. I. Molotkov, O. F. Petrov, Y. P. Gidzenko, S. K. Krikalev, W. Shepherd, A. I. Ivanov, M. Roth, H. Binnerbruck, J. A. Goree, and Y. P. Semenov, New Journal of Physics **5**, 33 (2003).
- <sup>7</sup>M. Klindworth, A. Piel, A. Melzer, U. Konopka, H. Rothermel, K. Tarantik, and G. E. Morfill, Phys. Rev. Lett. **93**, 195002 (2004).
- <sup>8</sup>C. Schmidt, O. Arp, and A. Piel, Phys. Plasmas **18**, 013704 (2011).
- <sup>9</sup>P. K. Shukla and A. A. Mamun, *Introduction to Dusty Plasma Physics* (Institute of Physics Publishing, Bristol, 2002).
- <sup>10</sup>G. E. Morfill and A. V. Ivlev, Rev. Mod. Phys. **81**, 1353 (2009).
- <sup>11</sup>A. Bouchoule, *Dusty Plasmas: Physics, Chemistry and Technological Impacts in Plasma Processing* (John Wiley & Sons, 1999).
- <sup>12</sup>G. M. Jellum and D. B. Graves, Journal of Applied Physics **67**, 6490 (1990).
- <sup>13</sup>P. Belenguer, J. Blondeau, L. Boufendi, M. Toogood, A. Plain, A. Bouchoule, C. Laure, and J. P. Boeuf, Phys. Rev. A **46**, 7923 (1992).
- <sup>14</sup>L. Boufendi, J. Gaudin, S. Huet, G. Viera, and M. Dudemaine, Applied Physics Letters **79**, 4301 (2001).
- <sup>15</sup>M. Schulze, A. von Keudell, and P. Awakowicz, Plasma Sources Science and Technology **15**, 556 (2006).
- <sup>16</sup>E. Schüngel, S. Mohr, S. Iwashita, J. Schulze, and U. Czarnetzki, J. Phys. D: Appl. Phys. **46**, 175205 (2013).
- <sup>17</sup>N. Bilik, R. Anthony, B. A. Merritt, E. S. Aydil, and U. R. Kortshagen, Journal of Physics D: Applied Physics **48**, 105204 (2015).
- <sup>18</sup>T. Wegner, A. M. Hinz, F. Faupel, T. Strunskus, H. Kersten, and J. Meichsner, Applied Physics Letters **108**, 063108 (2016).
- <sup>19</sup>P. R. i Cabarrocas, Y. Djeridane, T. Nguyen-Tran, E. V. Johnson, A. Abramov, and Q. Zhang, Plasma Physics and Controlled Fusion **50**, 124037 (2008).
- <sup>20</sup>L. Boufendi and A. Bouchoule, Plasma Sources Science and Technology **3**, 262 (1994).
- <sup>21</sup>E. Kovacevic, I. Stefanovic, J. Berndt, Y. J. Pendleton, and J. Winter, The Astrophysical Journal **623**, 242 (2005).
- <sup>22</sup>Y. Watanabe, Journal of Physics D: Applied Physics **39**, R329 (2006).
- <sup>23</sup>J. Beckers, W. W. Stoffels, and G. M. W. Kroesen, Journal of Physics D: Applied Physics **42**, 155206 (2009).
- <sup>24</sup>F. Greiner, J. Carstensen, N. Köhler, I. Pilch, H. Ketelsen, S. Knist, and A. Piel, Plasma Sources Science and Technology **21**, 065005 (2012).
- <sup>25</sup>I. Stefanovic, B. Sikimi, A. Aschinger, J. Berndt, E. Kovacevic, and J. Winter, Journal of Physics D: Applied Physics **48**, 385202 (2015).
- <sup>26</sup>F. M. J. H. van de Wetering, R. J. C. Brooimans, S. Nijdam, J. Beckers, and G. M. W. Kroesen, Journal of Physics D: Applied Physics **48**, 035204 (2015).
- <sup>27</sup>Y. Qin, U. R. Kortshagen, and E. S. Aydil, Journal of Physics D: Applied Physics **49**, 085203 (2016).
- <sup>28</sup>S. Groth, F. Greiner, B. Tadsen, and A. Piel, Journal of Physics D: Applied Physics **48**, 465203 (2015).
- <sup>29</sup>B. Tadsen, F. Greiner, and A. Piel, Physics of Plasmas **21**, 103704 (2014).
- <sup>30</sup>G. H. P. M. Swinkels, E. Stoffels, W. W. Stoffels, N. Simons, G. M. W. Kroesen, and F. J. de Hoog, Pure and Applied Chemistry **70**, 1151 (1998).
- <sup>31</sup>W. W. Stoffels, E. Stoffels, G. H. P. M. Swinkels, M. Boufnichel, and G. M. W. Kroesen, Phys. Rev. E **59**, 2302 (1999).
- <sup>32</sup>J. Carstensen, H. Jung, F. Greiner, and A. Piel, Phys. Plasmas **18**, 033701 (2011).
- <sup>33</sup>C. Killer, M. Mulsow, and A. Melzer, Plasma Sources Science and Technology **24**, 025029 (2015).
- <sup>34</sup>M. Klindworth, O. Arp, and A. Piel, J. Phys. D: Appl. Phys. **39**, 1095 (2006).
- <sup>35</sup>S. Mitic, M. Y. Pustynnik, E. Kovaevi, J. Berndt, L. Boufendi, and G. E. Morfill, Journal of Physics D: Applied Physics **45**, 335203 (2012).
- <sup>36</sup>C. Killer, M. Himpel, and A. Melzer, Review of Scientific Instruments **85**, 103711 (2014).
- <sup>37</sup>A. C. Kak and M. Slaney, *Principles of Computerized Tomographic Imaging* (IEEE Press, 1988).
- <sup>38</sup>E. Kovacevic, J. Berndt, T. Strunskus, and L. Boufendi, Journal of Applied Physics **112**, 013303 (2012).
- <sup>39</sup>R. Fisher, K. Avinash, E. Thomas, R. Merlino, and V. Gupta, Phys. Rev. E **88**, 031101 (2013).
- <sup>40</sup>O. Havnes, G. E. Morfill, and C. K. Goertz, Journal of Geophysical Research: Space Physics **89**, 10999 (1984).
- <sup>41</sup>I. Goertz, F. Greiner, and A. Piel, Phys. Plasmas **18**, 013703 (2011).
- <sup>42</sup>B. Tadsen, F. Greiner, S. Groth, and A. Piel, Physics of Plasmas **22**, 113701 (2015).
- <sup>43</sup>G. Pretzler, Z. Naturforsch. **46a**, 639 (1991).
- <sup>44</sup>C. Killer, "Abel inversion algorithm," Online (2013), MATLAB Central File Exchange.